Nano Energy 57 (2019) 791–803

Contents lists available at ScienceDirect

Nano Energy

journal homepage: www.elsevier.com/locate/nanoen

Full paper

The critical nanofluid concentration as the crossover between changed and unchanged solar-driven droplet evaporation rates

Jinliang Xu[a,b,*], Xin Yan[a], Guohua Liu[a], Jian Xie[a]

[a] Beijing Key Laboratory of Multiphase Flow and Heat Transfer for Low Grade Energy Utilization, North China Electric Power University, Beijing 102206, China
[b] Key Laboratory of Condition Monitoring and Control for Power Plant Equipment of Ministry of Education, North China Electric Power University, Beijing 102206, China

ARTICLE INFO

Keywords:
Solar energy
Critical nanofluid concentration
Droplet
Heat transfer
Shadow effect
Renewable energy

ABSTRACT

The challenge of the nanofluid solar energy harvesting lies in the strong coupling between nanoparticles generated heat and flow/temperature fields in various length and time scales. In this paper, the solar-driven evaporation of nanofluid droplet is investigated. The droplet evaporation rates behave a sharply increased regime and a constant regime when crossing a critical nanofluid concentration of $c_{i,cr} = 10$ ppm. We decouple the total solar energy absorption into two parts in terms of the optical bands, and the whole droplet into two spatial domains. Our study reveals a small length scale starting from contact line to behave higher temperature and larger temperature gradient there, newly recognized as a boundary layer effect. Correspondingly, a contact line region CLR is defined, while the remain is the bulk volume region BVR. The observed coffee-ring behaves a self-assembly of nanoparticles in CLR. We found that even though CLR is two magnitudes smaller compared to the whole droplet, it dominates almost all of the electromagnetic energy absorption, while BVR contributes almost all of the infrared energy absorption. Our finding successfully explains the two regimes of droplet evaporations. With increase of initial nanofluid concentrations, the droplet evaporation rates are raised due to more heat generation induced by enhanced nanoparticles deposition in CLR. The increased evaporation rates stop at a critical concentration of 10 ppm, corresponding to sufficient nanoparticles deposition. Beyond the critical condition, extra nanoparticles are hidden beneath the effective nanoparticles layers to cause unchanged evaporation rate. The present work is useful to develop novel solar steam generation device. The evaporation induced coffee-ring can be regarded as a novel “fabrication” method of nanostructure for plasmonic heating. The pure water evaporation of liquid film or droplet on a prepared coffee-ring array offers great convenience for solar energy utilization.

1. Introduction

The interaction between electromagnetic fields and free electrons in metals induces the surface plasmon resonance (SPR). The electric field components of light excite the free electrons in metals to produce collective oscillations. Such interaction involves both the surface plasmon-polariton (SPP) that takes place along the metal surfaces, and the localized surface plasmon resonance (LSPR), which is confined in a local space around an isolated nanoparticle. The plasmonic effect brings to a broad range of applications in biology [1], chemistry [2], information [3], bio-imaging [4], sensing [5], surface-enhanced Raman scattering (SERS) [6], chemical reactions [7], cancer treatment [8] and solar energy extraction [9–11]. Based on Maxwell's equations, the Mie scatting theory can be used to investigate the light/nanoparticle interaction, which is influenced by metal material, shape, surrounding medium, nanoparticle size and gap [12–14]. Recent advances in the synthesis, assembly, characterization, and theories of metal nanostructures open a new way to the plasmonic applications. The theory of plasmon resonance is still challenging due to the complex plasmon-coupling with surrounding medium.

Great attention has been paid to the solar energy extraction using nanofluid [10,15]. Especially, solar steam generation opens a new way of solar-thermal conversion and seawater desalination [10,16]. Table 1 lists some recent studies on solar energy harvesting using nanofluid [17–27], showing scatted data of optimal nanofluid concentrations. This contradiction inspired us to investigate the multi-physical-field-coupling between electromagnetic field, temperature and flow fields. Let's examine what happens for nanofluid without light irradiation first:

* Corresponding author at: Beijing Key Laboratory of Multiphase Flow and Heat Transfer for Low Grade Energy Utilization, North China Electric Power University, Beijing 102206, China.
E-mail address: xjl@ncepu.edu.cn (J. Xu).

https://doi.org/10.1016/j.nanoen.2019.01.013
Received 25 November 2018; Received in revised form 28 December 2018; Accepted 3 January 2019
Available online 04 January 2019
2211-2855/

Nomenclature

c	nanofluid concentration, ppm
c_i	initial nanofluid concentration, ppm
c_v	vapor concentration near droplet surface, kg/m^3
$c_{i,cr}$	initial critical nanofluid concentration, ppm
c_{BVR}	nanofluid concentration in BVR, ppm
d_p	diameter of gold nanoparticle, nm
D	droplet contact diameter, mm
h_{ring}	coffee-ring height, nm
h	Planck constant, $h = 6.626 \cdot 10^{-34}$ J s
h_{fg}	latent heat of vaporization, kJ/kg
$k_{a\lambda}$	spectral absorption coefficient, cm^{-1}
L_c	circumferential length, m
$\boldsymbol{n}$	normal vector of the droplet surface
n_t	total number of nanoparticles in droplet
n_{BVR}	number of nanoparticle in BVR
n_{CLR}	number of nanoparticle in CLR
q_r	radiation flux density of solar simulator, W/m^2
Q_d	heat generation power in droplet, W
Q_s	heat release from droplet surface to environment, W
Q_{el}	electromagnetic energy in visible region absorbed by nanoparticles, W
Q_{ir}	infrared energy absorbed by water, W
$Q_{el,BVR}$	electromagnetic energy absorbed by nanoparticles in BVR, W
$Q_{el,CLR}$	electromagnetic energy absorbed by nanoparticles in CLR, W
S_{ring}	coffee-ring cross-section area, nm^2
t	time, s
T	temperature, ˚C
T_c	contact line temperature, ˚C
T_i	droplet surface temperature, ˚C
T_{IR}	temperature measured by IR camera, ˚C
T_1, T_2, T_3	three temperatures on droplet surface, ˚C
ν	vibrational frequency, rad/s
V	droplet volume, μL
V_i	initial droplet volume, μL
V_p	nanoparticle volume, nm^3
$V_{\tau e}$	droplet volume at τ_e, μL
V_{ring}	coffee-ring volume, nm^3
$V_{ring,p}$	nanoparticles volume in coffee-ring, nm^3
w_{ring}	coffee-ring width, μm

Greek Symbols

β	angle in Fig. 6b
δ	circumferential length of CLR, m
$\Delta\tau$	evaporation time after breakage of liquid film on glass substrate, s
η_{el}	nanoparticles energy contribution factor
θ	droplet contact angle
θ_i	initial droplet contact angle
λ	wavelength, nm
ρ_f	density of liquid, g/cm^3
ρ_p	gold nanoparticle density, g/cm^3
τ_e	droplet evaporation time in CCD mode, s
τ_λ	spectral transmittance
φ	porous porosity of coffee-ring

Subscripts

i	initial time
λ	spectral
BVR	bulk volume region
CLR	contact line region
ring	coffee-ring
p	nanoparticle

Table 1
The nanofluid concentration in literature.

references	base fluid	nanoparticles			best concentration
		species	size (nm)	concentration	
Wang et al. [17]	Water	Au	13	5, 10, 23.5, 41.7, 87.2, 178.0 ppm	178.0 ppm
Yousefi et al. [18]	Water	Al_2O_3	15	0.2, 0.4 wt%	0.2 wt%
Yousefi et al. [19]	Water	MWCNT	10–30	0.2, 0.4 wt%	0.4 wt%
Taylor et al. [20]	Water	Ag	30	0.004, 0.04 vol%	0.004 vol%
Bandarra et al. [21]	Water	Ag	10	1.62, 3.25, 6.5 ppm	6.5 ppm
He et al. [22]	Water	Cu	25, 50	0.01, 0.02, 0.04, 0.1, 0.2 wt%	0.1 wt%
de Risi et al. [23]	Nitrogen gas	CuO + Ni		0.01–0.3 vol%	0.3 vol%
Zhang et al. [24]	Water	Au	10–30	0.00028, 0.0007, 0.0014, 0.0028, 0.0112 wt%	0.0112 wt%
Jamal-Abad et al. [25]	Water	Cu	35	0.05, 0.1 wt%	0.1 wt%
Kundan and Sharma [26]	Water	CuO	80	0.005, 0.05 wt%	0.005 wt%
Karami et al. [27]	Water	CNT	Diameter:10 nm;Length:5–10 μm	5, 10, 25, 50, 100, 150 ppm	150 ppm

(1) *Multiscale behaviors:* Several spatial/temporal scales are involved in a nanofluid system [28]. (2) *Various forces interactions:* Various interaction forces between nanoparticles exist in nanofluid [29]. Van der Waals forces arise between all molecules and particles, whether in air (vacuum) or in liquid. Magnetic and electrostatic forces, repulsive steric, confining or jamming forces, solvation, structural and depletion forces, convective forces and capillary forces are other examples. (3) *Brownian movement:* The Brownian movement of particles is caused by all the impulses of fluid molecules on particles surface [28]. The above effects redistribute the nanoparticles and alter the gap of nanoparticles to influence the nanofluid transport properties.

The problem becomes more complicated for solar energy harvesting using nanofluid, in which the excited electrons energy is dissipated into thermal energy to be received by base liquid. The challenge lies in the strong coupling between the spatial-time dependent nanofluid concentrations and the flow/temperature fields. When a light irradiates nanofluid, nanoparticles are redistributed to alter the interparticle gaps, influencing the heat generation. What's more, nanoparticles have a tendency to aggregate, forming larger particles cluster to influence the solar energy absorption [30,31]. Recently, Amani et al. [32] dealt with the nanofluid heat transfer (channel heating) using the two-phase mixture model, considering the heterogeneity of concentration due to the effects of shear rate, viscosity gradient, thermophoresis and Brownian motion on the nanoparticles diffusion.

The droplet evaporation has been widely investigated due to its applications in inkjet printing, hot-spot cooling, bio-sensing and DNA

mapping [33–35]. There are two droplet evaporation modes: constant contact diameter (CCD) mode with a pinned contact line, and constant contact angle (CCA) mode with varied contact diameters [36]. The CCD mode is paid more attention in the literature, during which the evaporation rate is a function of contact angles [33]. The linear droplet evaporation only takes place at smaller initial contact angle such as $\theta_i < 45^\circ$, while the non-linear behavior occurs at larger initial contact angle [33,34]. A complete droplet evaporation leaves nano-particles on the substrate to form the coffee-ring pattern. The coffee-ring formation is balanced by two opposite effects [37]. The radial flow from droplet center to contact line enhances the particle deposition. On the other hand, the Marangoni flow due to the surface tension gradient over the whole droplet surface suppresses the coffee-ring formation [35].

Even though the droplet evaporation has been extensively studied [38–40], the light/solar driven sessile droplet evaporation of plasmonic nanofluid is investigated for the first time in this paper. The evaporation rates are found to behave an increase regime and a constant regime when crossing a critical concentration of ~10 ppm. A decoupling strategy is proposed. First, the total light energy extraction includes an infrared energy part and an electromagnetic energy part in visible region. The two kinds of energy are separated in terms of the energy optical bands. Thus, one can identify the nanoparticles contribution to the heat generation. Second, the whole droplet is decoupled into a bulk volume region BVR and a contact line region CLR. The latter has a small length scale. After calculating the electromagnetic energy by the Mie scatting theory using the transient nanofluid concentrations in BVR, we conclude that almost all the electromagnetic energy generation is contributed by CLR nanoparticles. The two regimes of droplet evaporation correspond to insufficient and extra nanoparticles deposition in CLR coffee-ring for heat generation, respectively. The new finding of this paper inspires us to develop novel solar driven water evaporation devices using pure water on the formed coffee-ring pattern having stacked nanoparticles.

2. Materials and methods

2.1. Experimental setup

Fig. 1 shows an apparatus image of the experiment. A nanofluid droplet in the volume range of $1.72 - 2.24\,\mu L$ was generated by a needle, which was driven by a syringe pump. The droplet could be separated from the needle tip and deposited on a glass substrate above a sample supporting glass cylinder. Transmittance of the glasses is above 90% in visible light region, thus the glass passes the light energy

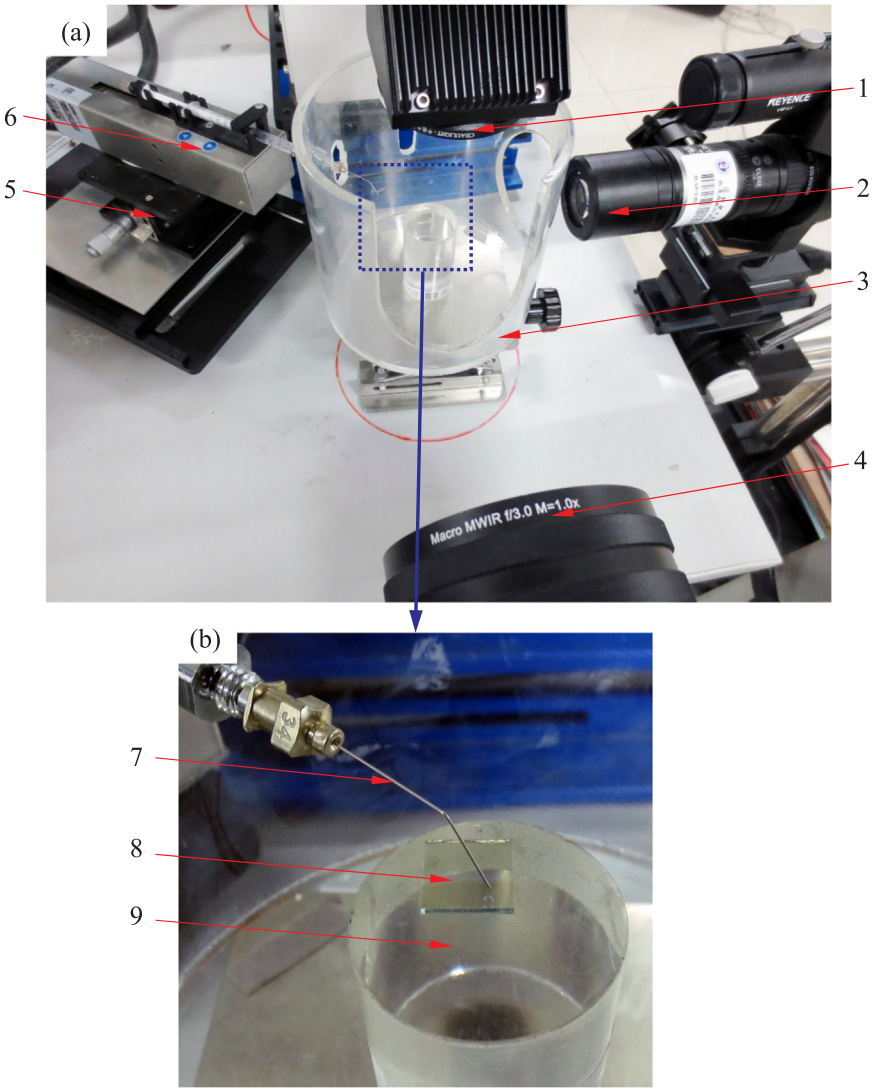

Fig. 1. Experimental setup (a: photograph of experimental setup, 1, Xenon lamp; 2, high-speed camera with resolution of 4.7 μm/pixel; 3, PMMA glass cloak; 4, high-speed IR camera, 5, XYZ axis platform; 6, micro-syringe pump. b: enlarged liquid injector/needle package and glass supporting substrate, 7, needle; 8, glass substrate; 9 sample supporting glass).

without generating heat itself. The glass thermal conductivity is ~1 W/(mK), which is sufficiently low to prevent heat leakage via the glass. The light induced droplet heating causes the droplet temperature rise and evaporation. The light source is a solar simulator (CEL-S500). The spectrum of the Xenon lamp adapted with an AM1.5 filter well matches the solar spectrum in visible light region (see Fig. S1 in Supplementary Information). The droplet was placed in a PMMA cloak to prevent it from being affected by disturbed air. Several holes on the cloak body directly exposes the droplet in front of a high-speed camera and an infrared (IR) camera for accurate measurements of droplet dynamics and surface temperatures. The high-speed camera and IR camera were synchronized together. The recording rates of both cameras was 20 Hz, which is sufficiently fast to track the droplet evolution. The room temperature was controlled as 25 ± 3 °C with an air humidity of 30 ± 3% (see Supplementary Information for measurement uncertainties).

2.2. Gold nanofluids

The gold chloride hydrate ($HAuCl_4$, Au ≥ 49%) and tri-sodium citrate ($Na_3C_6H_5O_7$, 99.8%) were purchased from Sigma-Aldrich. The $HAuCl_4$ reacts with $Na_3C_6H_5O_7$ in boiling water to form the gold nanofluid having wine-red color [15]. After ultra-sonic oscillation, the nanofluid stabilization is enhanced without particles coalescence and deposition for a long time. The nanoparticles are in sphere shape and behave a quasi-normal-distribution with an average diameter of 18.87 nm by analyzing 138 particles. Usually, the nanofluid is thought to be stabilized if the absolute Zeta potential is larger than 60 mV [41]. Here, the measured Zeta potential is − 67.5 mV to display excellent stabilization (see Fig. S2 in Supplementary Information). The absorption coefficient and transmittance characterize the nanofluid optical performance. Fig. 2a shows the increased absorption coefficients with rising nanofluid concentrations from $c_i = 0$ (pure water) to $c_i = 100$ ppm. The spectral absorption coefficient $k_{a\lambda}$ holds a peak value due to the enhanced plasmonic effect when crossing a resonance wavelength λ, which is 520 nm for all the nanofluids tested here, matching the predicted wavelength with a particle size of 19 nm [42]. The variation trend of the transmittance τ_λ versus wavelength λ is inverse to the absorption coefficient. The values of τ_λ are decreased with increase of c_i, and the minimum τ_λ occurs at λ = 520 nm (see Fig. 2b). The nanofluids enhance the absorption in the visible light region. At a higher concentration such as $c_i = 100$ ppm, the peak absorption coefficient $k_{a\lambda}$ attains 1.26 cm^{-1} and the transmittance reaches $\tau_\lambda = 5.3\%$ at λ = 520 nm, meaning that only 5.3% of the light energy penetrates through the test sample. The optical measurement was performed in a pool nanofluid. Later we will see that the light induced droplet evaporation changes the performance shown in Fig. 2.

3. Results and discussion

3.1. Droplet evaporation dynamics and evaporation rates

The droplet evaporation mode (CCD or CCA) and the transition from one to another depend on the balance between contact angle and contact angle hysteresis. For larger contact angle hysteresis, the contact line is pinned on the surface to result in the CCD mode. Otherwise, a droplet prefers to choose the CCA mode to minimize the surface energy between solid and liquid [43]. Fig. 3a shows the effect of different heating methods, and Fig. 3b shows the effect of different nanofluid concentrations for solar heating. Both indicate a constant contact diameter (CCD) stage, covering a time period of τ_e, followed by a contracted liquid film evaporation stage, covering a time period of $\Delta\tau$. Here, τ_e is defined as the time from the start of heating to the end of CCD, in which D is unchanged but θ decreases.

The transition between the two stages is related to the energy barrier between glass surface and droplet, and the line tension force at contact line. The energy barrier increases following the start of heating but remains constant when the particle deposition on the surface is complete. However, the line tension force rises with the evolution of droplet evaporation. At the end of τ_e, the line tension force is sufficiently large which cannot be balanced off the energy barrier at contact line. Thus, the liquid film on substrate is broken to form the contracted liquid film on a local area (see Fig. 3c). The CCD mode deposits nanoparticles to form the coffee-ring during $0 - \tau_e$, while the contracted liquid film evaporation creates the nanoparticles island during $\tau_e - \tau_e + \Delta\tau$ (see Fig. 3d). We note that τ_e lasts a large percentage of the whole drop lifetime, leaving a very small residual drop volume V_{τ_e} at $t = \tau_e$. For solar heating with $q_r = 1400$ W/m^2 and $c_i = 50$ ppm, $\tau_e/(\tau_e + \Delta\tau)$ and V_{τ_e}/V_i are 93.5% and 2.6% respectively, where V_i is the initial drop volume at $t = 0$. For latter presentation, the evaporation results are only presented in the period of $0 - \tau_e$. The experiments of solar heating induced droplet evaporation were performed with natural light, solar incident radiation flux density of $q_r = 800$ W/m^2 and 1400 W/m^2. The ranges of c_i and V_i are $0 - 100$ ppm and

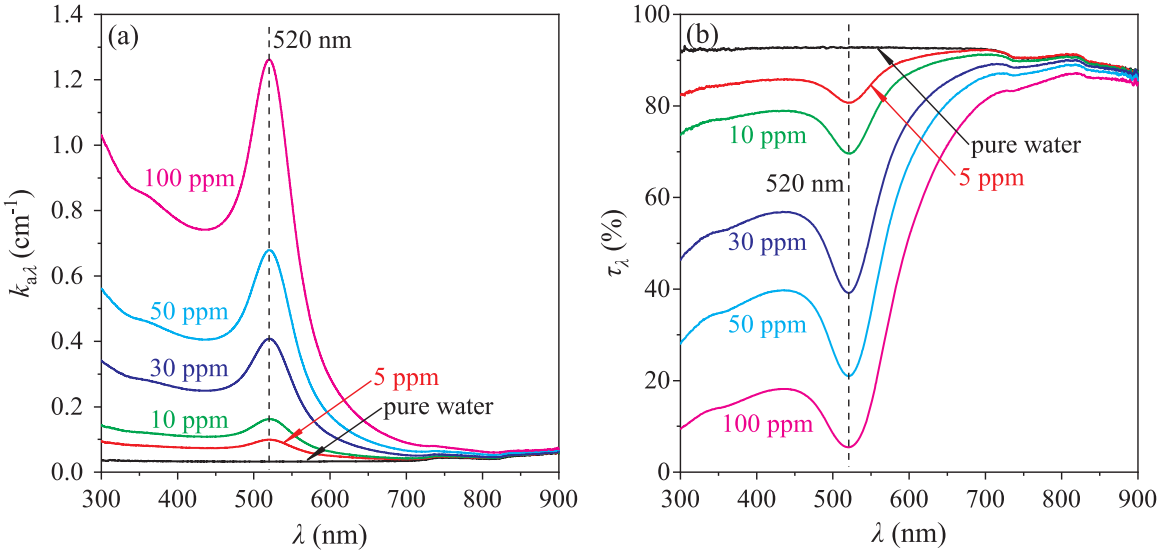

Fig. 2. Characterization of nanofluid with gold nanoparticles (a: absorption coefficient versus wavelength; b: transmittance spectrum versus wavelength. Curves are shown for different nanofluid concentrations.).

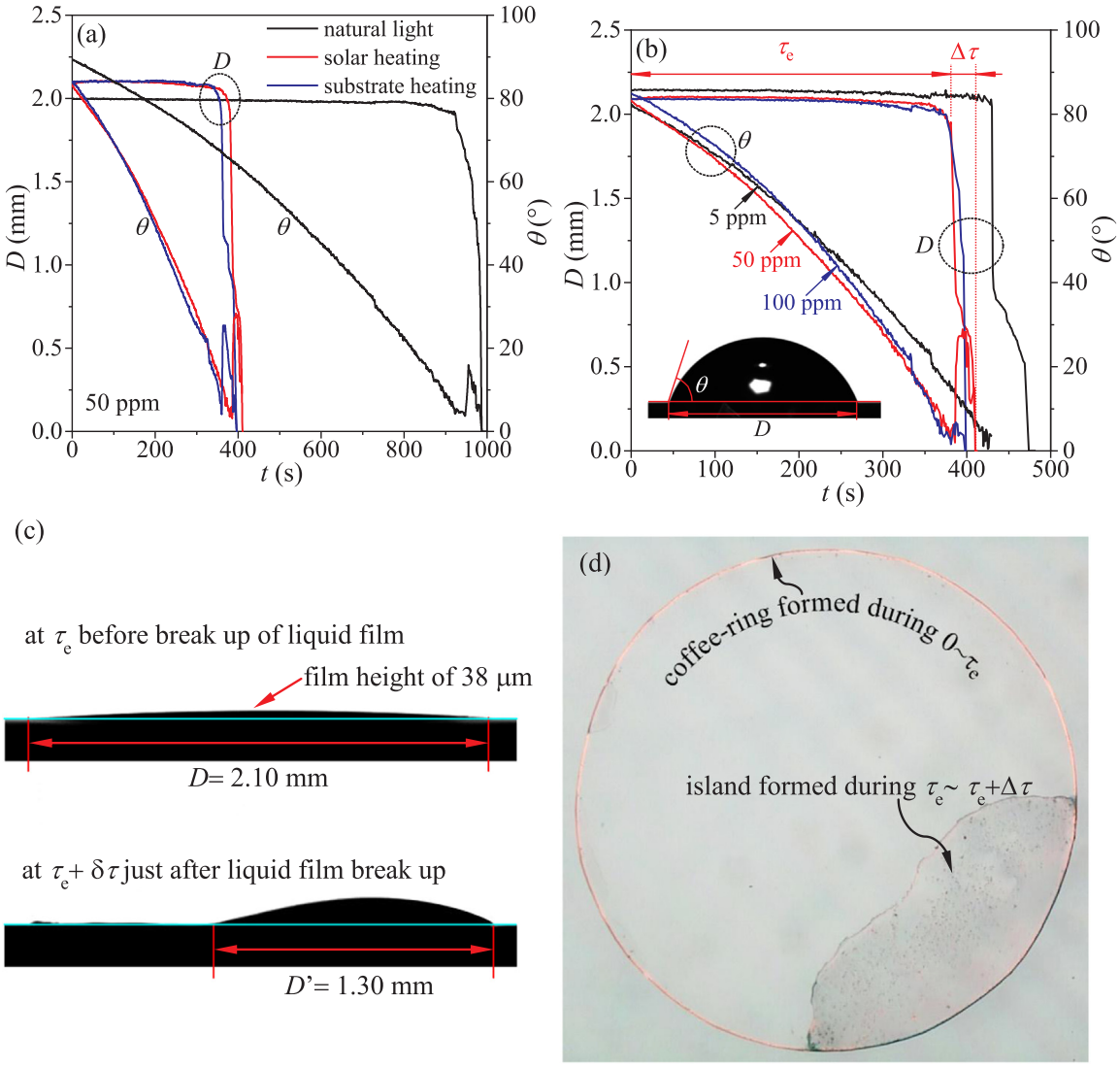

Fig. 3. Overall gold nanofluid drop evaporation dynamics (a: contact diameter D and contact angle θ for c_i = 50 ppm at substrate heating with T_w = 35.7 °C, solar heating with q_r = 1400 W/m^2 and natural light evaporation; b: effect of c_i on D and θ for V_i = 2.00 ± 0.04 μL and q_r = 1400 W/m^2, showing the CCD mode for solar heating induced nanofluid drop evaporation, $\tau_e/(\tau_e+\Delta\tau)$ = 93.5%; c: liquid film break up process; d: coffee-ring and nanoparticles island formed in different stages).

1.72 − 2.24 μL, respectively. Two new findings are summarized here: (1) *Constant droplet evaporation rates* (see Fig. 4a), and (2) *Two regimes of droplet evaporation rates* (see Fig. 4b-c).

The solar heating induced droplet evaporation obeys the linear law of $V-t$. Most of nanoparticles move to the contact line region and deposit there in the early stage of solar heating, leaving a small percentage of nanoparticles in the bulk volume region. The re-assembly of nanoparticles causes dominant plasmonic heat generation in the contact line region. Thus, the plasmonic heat generation is weak in the bulk volume region, even though the droplet volume reduces and the instantaneous nanoparticles concentration increases during evaporation (see detailed analysis in the following sections). In contrast, the substrate heating generates non-linear droplet evaporation (see inserts 1 and 2 in Fig. 4a).

Fig. 4b shows droplet evaporation time τ_e versus initial droplet volume V_i at different initial nanofluid concentrations c_i, demonstrating the scattered distribution. The data are presented in a different way shown in Fig. 4c to demonstrate that with continuous increase of c_i from 0 to 100 ppm, the droplet $V_i/\tau_e - c_i$ curves behaves a rising evaporation rate regime and a constant evaporation regime. The V_i/τ_e characterizes the overall droplet evaporation rate, which is identical to the slope of $V-t$ curve due to the linear relation shown in Fig. 4a. The two regimes are interfaced at a critical concentration of about 10 ppm, which is true for both the natural light heating and solar heating at q_r = 800 W/m^2, 1400 W/m^2 and others. Fig. 4c concludes the two regimes of droplet evaporation rates when crossing a critical nanofluid concentration.

3.2. Identification of CLR and BVR based on droplet surface temperatures

In order to understand the critical concentration phenomenon, the droplet dynamics and heat generation mechanism are analyzed in the following sections. The IR camera detects the temperatures containing both droplet domain and air domain (see Fig. 5a). The droplet interface is identified based on the different responses to the signals received from liquid region and air region. T_i is the droplet interface temperature beyond which the temperatures sharply rise in air (see Fig. 5a). Because it is of our interest in droplet dynamics, Fig. 5b-c only presents droplet surface temperatures excluding the air region. The solar heating and substrate heating generate different temperature fields. For solar heating, temperatures are quasi-uniform except the contact line region to exhibit enclosed isothermal pattern (see Fig. 5b). For substrate heating, temperature stratification is presented which qualitatively agrees well with Fukatani et al. [44] and Chandramohan et al. [45] (see Fig. 5c).

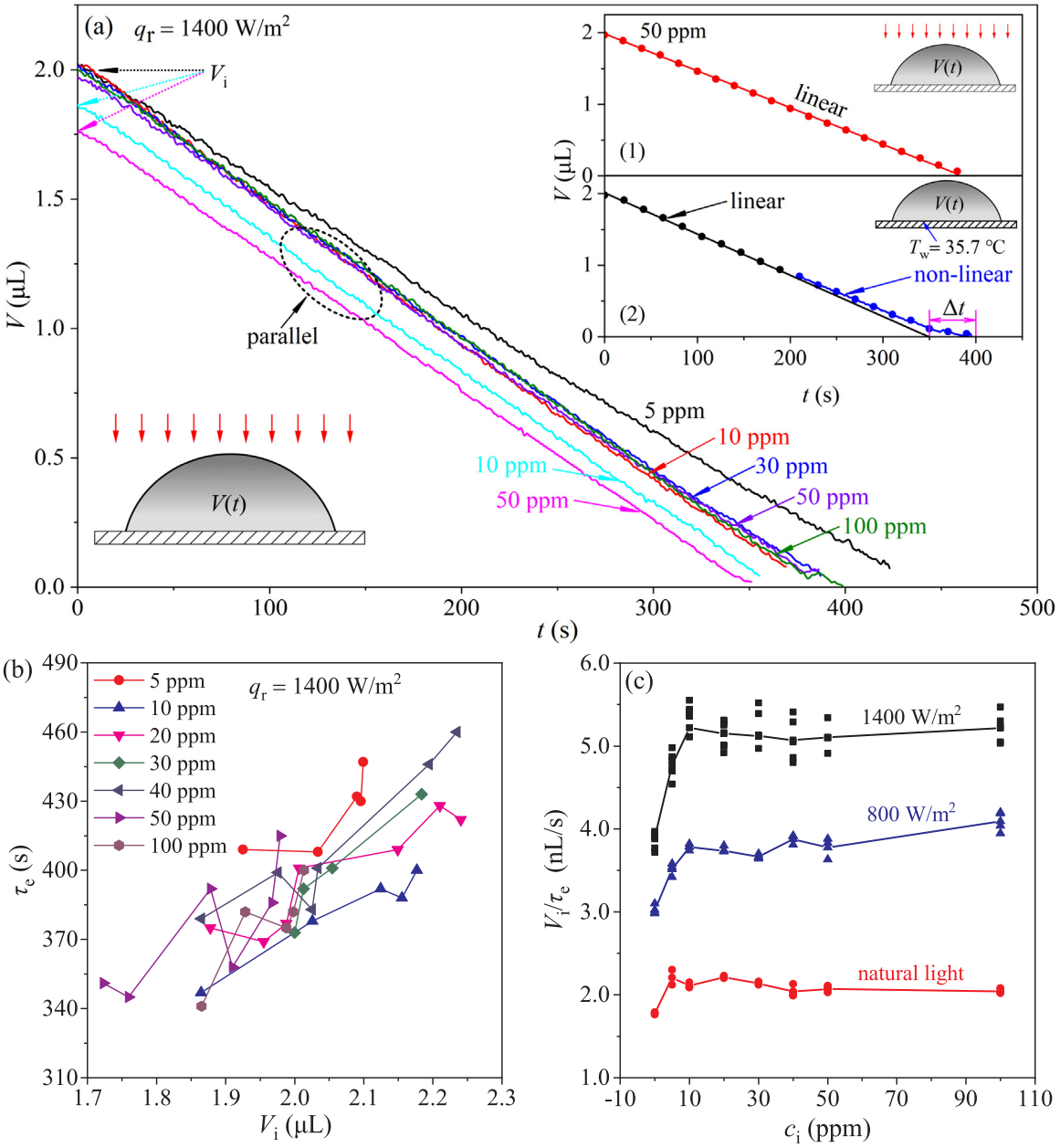

Fig. 4. Performance of solar heating induced droplet evaporation (a: linear relationship between residual droplet volume V versus time t, showing constant dynamic drop evaporation rate (dV/dt) for different initial nanofluid concentrations beyond c_i = 10 ppm; b: scattered droplet lifetime for different initial droplet volume; c: the two regimes of droplet evaporation rates interfaced at a critical concentration of 10 ppm).

The effect of nanofluid concentrations on transient contact line temperatures T_c is shown in Fig. 6a, exhibiting the elevated T_c with c_i increased from 0 to 10 ppm. The T_c curves are almost coincident with each other when c_i > 10 ppm. Fig. 6b shows higher T_c at the contact line than other three points where arc angle β is 30°. Here β is referenced to the horizontal plate. The droplet surface temperatures are further examined along the whole circumferential direction, with the original point O defined at the droplet apex and L_c representing the stretched length along the droplet circumference (see Fig. 6c). Two regions are identified: a higher temperature region within δ, and a flat temperature region beyond δ, where δ is the length from the contact line to the point at the onset of unchanged temperatures. This behavior lasts in the whole droplet lifetime, during which L_c is shortened continuously due to the decreased droplet height. Thus, two spatial regions are defined: a contact line region (CLR) corresponding to the arc length δ, and a bulk volume region (BVR) corresponding to the surface except the arc length δ. The small length scale of δ having higher temperatures and larger temperature gradient is newly recognized as a boundary layer effect for light-driven evaporation, which cannot occur in substrate heating induced droplet evaporation.

We highlight the droplet evaporation difference between the two heating methods. For solar heating, the droplet surface temperature is uniform except the contact line region. The radial flow from droplet center to contact line induces nanoparticles deposition near the contact line to enhance heat generation there. Thus, the contact line region CLR behaves higher temperature and larger temperature gradient, which is a local effect. In contrast, for substrate heating, the heat conduction generates the temperature gradient over the whole droplet, not in a local region.

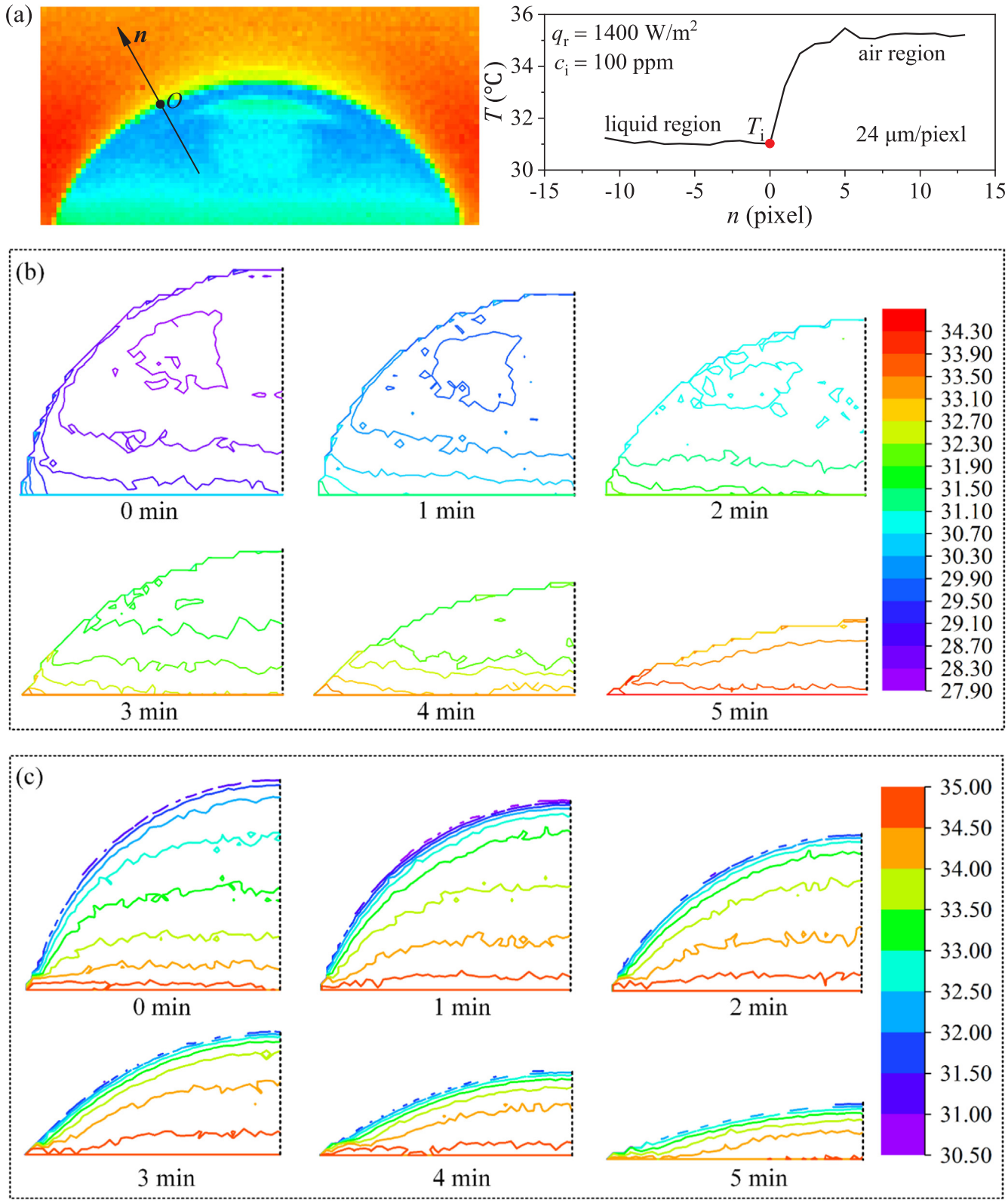

Fig. 5. The spatial distribution of drop surface temperature, showing different nature between solar heating and substrate heating (a: identification principle of temperatures in air region and liquid region; b: isothermal diagram of solar heating induced drop evaporation for c_i = 50 ppm and q_r = 1400 W/m^2; c: isothermal diagram of substrate heating induced drop evaporation for c_i = 50 ppm and T_w = 35.7 °C).

3.3. Re-assembly of nanoparticles in CLR and BVR

The ratio of the CLR volume to the total volume of droplet can be scaled by $(\delta/L_c)^3$. The magnitude of $(\delta/L_c)^3$ is in the range of 0.6 − 3.5% for all the droplets with c_i from 0 to 100 ppm, demonstrating the CLR volume two magnitudes smaller compared to the whole droplet. Fig. 7a illustrates the decreased $(\delta/L_c)^3$ versus time with c_i = 0, 5 ppm and 10 ppm, except a slight recovery of $(\delta/L_c)^3$ in latter

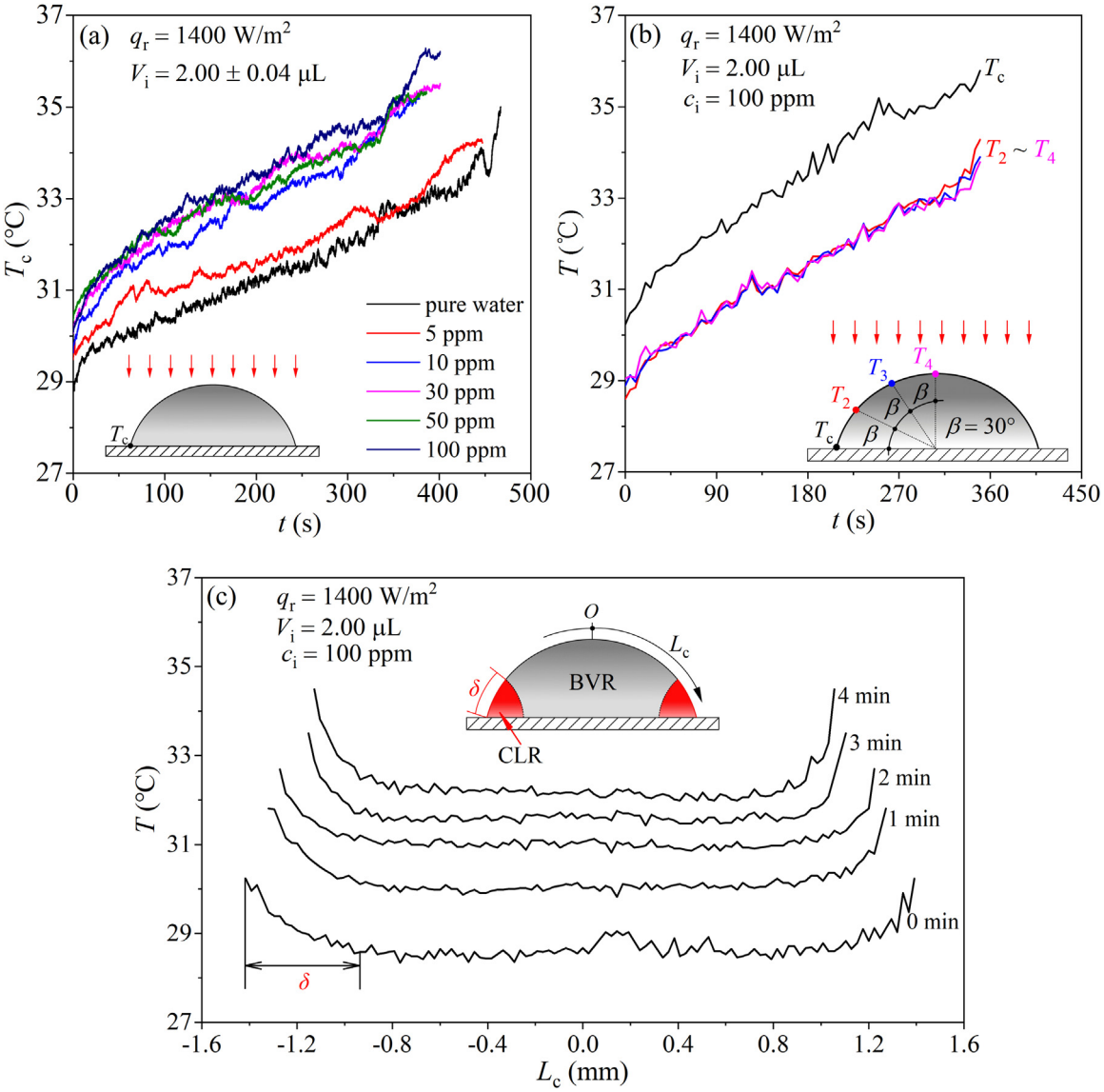

Fig. 6. The time-spatial dependent droplet surface temperatures (a: dynamic temperatures at contact line showing weakly dependent on initial nanofluid concentrations for $c_i > 10$ ppm; b: dynamic surface temperatures at different locations; c: characterization of CLR and BVR based on continuous surface temperature measurements).

evaporation stage with $c_i > 10$ ppm. Regarding the effect of c_i on $(\delta/L_c)^3$, Fig. 7b shows the flat distribution beyond the critical concentration of 10 ppm.

The nanoparticles motion and deposition are controlled by two mechanisms: the Marangoni flow and the radial flow. Our theoretic analysis shows that for solar heating induced droplet evaporation, the Marangoni flow cannot be developed over the whole droplet due to quasi-uniform droplet temperature. However, the radial flow is success to entrain nanoparticles traveling from droplet center to CLR. The Marangoni flow is only confined in a local region of CLR. Based on the theoretical analysis in Supplementary Information, the flow picture during the solar induced droplet evaporation is shown in Fig. 7c. Because the particles in droplet are nanoscale, which are too small to be used as the tracer particles for velocity measurement by PIV. Usually, micron-sized particles are needed as the tracer particles for PIV measurement.

Fig. 8a shows the coffee-ring patterns for c_i = 5 ppm, 30 ppm and 100 ppm. The coffee-ring can be considered as a self-assembly of nanoparticles during drop evaporation. Except the coffee-ring, the nanoparticles island exists to display random distribution due to random breakage of the thin liquid film at $t = \tau_e$. The width and height over the ring cross-section are termed as w_{ring} and h_{ring} respectively, whose values are shown in Fig. 8b, noting that the widths w_{ring} are almost the same (w_{ring} = 6.3 −7.0 μm) for different c_i, but the heights h_{ring} are increased with c_i from 5 ppm to 100 ppm. The coffee-ring has uniform cross-section along the circumferential direction (see P_1, P_2 and P_3 in Fig. 8a-b).

To explain Fig. 4c, one needs to estimate the heat generation in droplet, which is depended on nanoparticles distribution. For a droplet with a c_i, one can assume a uniform distribution of nanoparticles. However, nanoparticles are quickly redistributed under solar irradiation. The total number of particles is balanced in the two regions:

$$n_t = n_{CLR} + n_{BVR} \quad (1)$$

where n_t is the total number of nanoparticles, which is $n_t = c_i V_i/(\rho_p V_p)$, ρ_p is the gold density of 19.32 g/cm^3, V_p is the single nanoparticle volume, $V_p = \pi d_p^3/6$, n_{CLR} and n_{BVR} are the number of nanoparticles in CLR and BVR, respectively.

Because nanoparticles deposition occurs in the timescale one magnitude shorter than τ_e, a complete deposition can be assumed at the

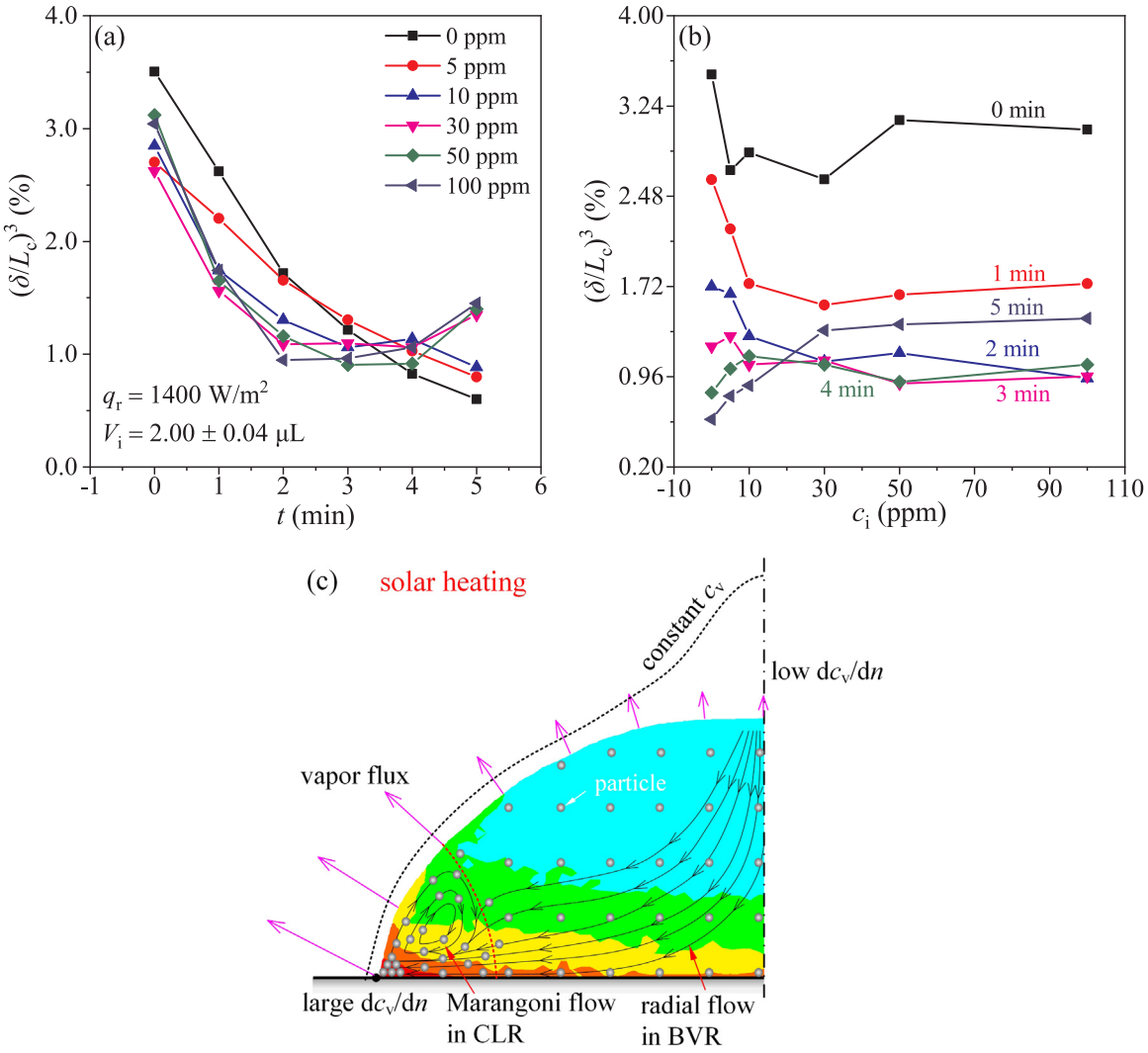

Fig. 7. Multiscale nature of the CLR volume to the whole droplet volume (a and b: effect of c_i and time t on $(\delta/L_c)^3$; c: flow field and temperature field in droplet as well as vapor concentration boundary near the droplet interface).

start of solar irradiation $t = 0$, which simplifies the heat generation analysis. Having the coffee-ring cross-section shown in Fig. 8b, the coffee-ring volume is $V_{ring} = \pi D S_{ring}$, where $S_{ring} = \int_0^{w_{ring}} z dx$. The porosity φ is the volume not occupied by nanoparticles divided by the total coffee-ring volume. For a randomly packed particles bed, φ is in the range of 0.359–0.375 [46]. Here, φ is averaged in the range to be 0.367, yielding the nanoparticles volume of coffee-ring as $V_{ring,p} = (1\text{-}\varphi)V_{ring}$ to have $n_{CLR} = V_{ring,p}/V_p$. The time-dependent nanofluid concentration in BVR is

$$c_{BVR} = \frac{(n_t - n_{CLR})\rho_p V_p}{V - V_{ring}} \tag{2}$$

where the drop volume V at any time t is calculated as

$$V = \frac{\cos^3\theta - 3\cos\theta + 2}{24\sin^3\theta}\pi D^3 \tag{3}$$

Even though n_t is quickly re-assigned to n_{CLR} and n_{BVR}, which are unchanged versus time, c_{BVR} is time-dependent due to the varied V during evaporation.

Table 2 shows nanoparticles redistribution in CLR and BVR. For any c_i, more than 90% of nanoparticles are deposited in CLR, leaving a small percentage of nanoparticles in BVR. The values of c_{BVR} significantly increase, and they are almost coincided with each other beyond the critical c_i of 10 ppm, except a gentle rise for c_i = 5 ppm (see Fig. 8c). The instantaneous nanoparticles concentration in BVR depends on the speed of nanoparticles deposition. For c_i = 5 ppm, the total number of nanoparticles is less to result in faster nanoparticles deposition compared with higher c_i cases, explaining the gentle rise of c_{BVR}. The balance of nanoparticles in CLR and BVR is determined by the coffee-ring volume measured by the surface profiler. For all the c_i cases, the coffee-ring width is almost the same, but the coffee-ring height is different. The measurement uncertainty depends on the ratio of coffee-ring height to its width. The smaller coffee-ring height corresponding to smaller c_i introduces larger uncertainty of the coffee-ring volume, explaining larger n_{BVR}/n_t = 8.7% compared with other cases (see Table 2).

3.4. Energy analysis in droplet

The heat generation in droplet (Q_d) represents the bulk effect, and the heat release from droplet surface to environment (Q_s) reflects the surface effect. The two heat loads are assumed to be equal due to the slow transition of the process. Q_s is calculated as

$$Q_s = \frac{\rho_f V_i h_{fg}}{\tau_e} \tag{4}$$

where V_i/τ_e is the droplet evaporation rate given in Fig. 4c, ρ_f is the

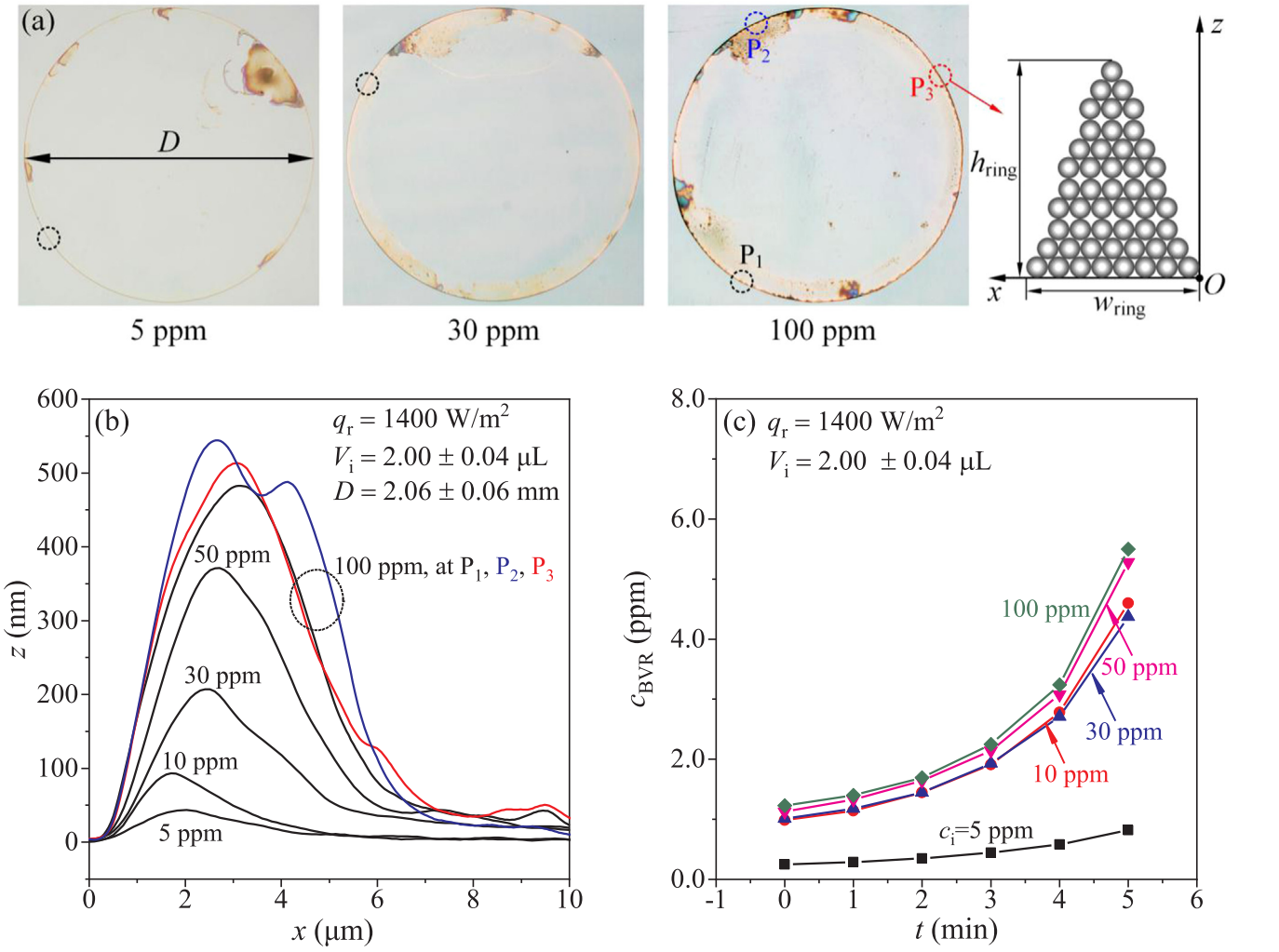

Fig. 8. Size measurement of coffee-ring cross-section (a: coffee-ring images characterized by ring height h_{ring} and width w_{ring}; b: effect of c_i on coffee-ring width and height; c: dynamic nanofluid concentrations in BVR based on the particle balance in CLR and BVR).

Table 2
The number of particles in CLR and BVR.

c_i (ppm)	n_t	n_{CLR}	n_{CLR}/n_t	n_{BVR}	n_{BVR}/n_t
5	1.54×10^8	1.49×10^8	96.8%	5.83×10^6	3.2%
10	3.12×10^8	2.85×10^8	91.3%	2.74×10^7	8.7%
30	9.49×10^8	9.21×10^8	97.0%	2.78×10^7	3.0%
50	1.49×10^9	1.46×10^9	98.0%	2.86×10^7	2.0%
100	2.93×10^9	2.89×10^9	98.6%	3.31×10^7	1.4%

nanofluid density, which is weakly dependent on particles concentration, h_{fg} is the latent heat of evaporation at the partial pressure of vapor near droplet interface. Q_d comes from infrared energy absorption by water Q_{ir} and electromagnetic energy in visible region absorbed by nanoparticles Q_{el} to have $Q_d = Q_{ir} + Q_{el} = Q_s$. Q_{el} is written as

$$Q_{el} = Q_s - Q_{ir} = \rho_f h_{fg} \left(\frac{V_i}{\tau_e}\bigg|_{c_i} - \frac{V_i}{\tau_e}\bigg|_{c_i=0} \right) \quad (5)$$

Having Eq. (5) and Fig. 4c, Q_{el} is scaled by the evaporation rate difference at a specific c_i and $c_i = 0$ (pure water). Q_{el} is assigned to $Q_{el,CLR}$ in CLR and $Q_{el,BVR}$ in BVR. Because nanoparticles in CLR are closely packed with each other to yield the shadowing effect, it is difficult to estimate $Q_{el,CLR}$, thus a heat generation model is established in Fig. 9a to calculate $Q_{el,BVR}$. The radiative transfer equation [47] and the Mie scattering theory [17] are used (see Supplementary Information). The analysis incorporates the dynamic nanofluid concentration given by Eq. (2).

Fig. 9b shows $Q_{el,BVR}/Q_{el}$ behaving constant versus time. This is because the light come from the top and the light project area is not changed during evaporation. The general trend is the increased $Q_{el,BVR}$ with increase of initial concentrations. With these results, the links between the heat generation in terms of the two optical bands and the two spatial domains are commented as follows:

Energy absorption in two optical bands: Q_d contains infrared energy absorbed by water (Q_{ir}) and electromagnetic energy in visible region absorbed by nanoparticles (Q_{el}). The nanoparticles energy contribution factor is defined as $\eta_{el} = Q_{el}/Q_d$, depending on q_r and c_i. For c_i larger than the critical value of 10 ppm, η_{el} is increased with q_r. In natural light environment, η_{el} is about 21%, but increased to 29% at $q_r = 1400\ W/cm^2$. η_{el} is sharply increased with increase of c_i before the critical concentration of 10 ppm (see Figs. 4c and 9c).

The energy contributions in two regions: Because CLR is two magnitudes smaller compared to the whole droplet, almost all the infrared energy is absorbed in BVR. However, BVR has negligible contribution for the electromagnetic energy absorption in visible region. For example, $Q_{el,BVR}/Q_{el}$ is ~0.06% at $q_r = 1400\ W/m^2$ and $c_i = 100$ ppm (see Fig. 9b). The CLR dominates the light absorption in visible region even though it is too small.

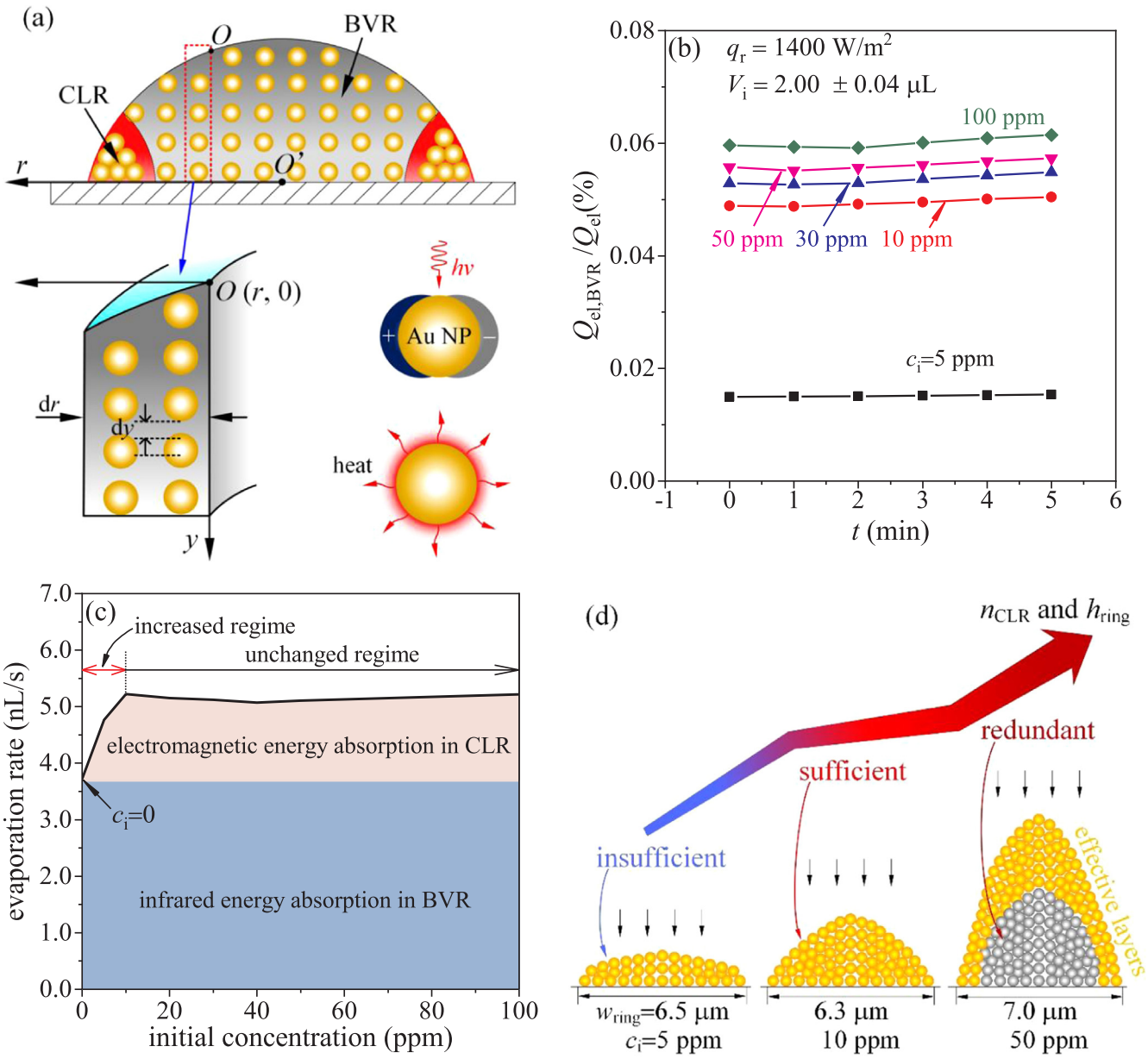

Fig. 9. Solar energy induced heat generation mechanisms (a: physical model for photo-thermal conversion in BVR; b: the ratio of electromagnetic energy in visible region induced heat generation in BVR to the solar energy absorption by total nanoparticles; c: the two regimes of droplet evaporation rates with V_i = 2.00 ± 0.04 μL and q_r = 1400 W/m^2; d: insufficient, sufficient and redundant nanoparticles deposited in coffee-ring to explain the critical concentration).

4. New findings and potential applications

The critical nanofluid concentration phenomenon can be summarized in Fig. 9c. The droplet evaporation rate is proportional to heat generation. The nanoparticles do not influence infrared energy absorption, but do affect visible light energy absorption to alter the evaporation rate. Most of nanoparticles are deposited in CLR in the early stage of droplet lifetime, causing a significantly non-uniform distribution of nanoparticles. For small c_i such as 5 ppm, the deposited particles are not sufficient to maximize the heat generation in CLR (see Fig. 9d). When c_i increases, the heat generation is enhanced to elevate the evaporation rate due to more particles deposition. The rising trend of evaporation rates stops when reaching a critical condition, at which there are sufficient nanoparticles in coffee-ring. The critical condition corresponds to a specific initial nanofluid concentration, which is ~10 ppm for gold nanoparticles with d_p = 18.87 nm in water. The critical initial concentration maybe affected by nanoparticles species, size and base liquid, which requires further investigation. For larger c_i beyond the critical value, even though more particles are deposited, the effective nanoparticles layers are not changed, resulting in constant evaporation rate and extra nanoparticles hidden beneath the effective particle layers. The latter can be called the shadowing effect of particles. Baffou et al. [48] showed that, when two d_p = 50 nm gold particles are irradiated by visible light, the absorption cross-section of the lower nanoparticle is ~36% of the above one, pointing out a clear shadowing effect of the upper sphere over the lower one. Based on Baffou et al. [48], we infer that 5–6 nanoparticles layers in our cases are efficient for heat generation.

The new findings of this paper can be summarized as: (1) maximum droplet evaporation rate can be reached at a critical nanofluid concentration of 10 ppm, (2) the bulk volume region has neglectable contribution to the heat generation in visible region, (3) the infrared energy absorption is identical no matter whether nanoparticles are used or not. These findings give a new clue to develop novel solar steam

generator for solar-thermal power conversion or seawater desalination. Two experiences can be learned from our present work. First, the droplet evaporation induced coffee-ring is a new fabrication method to deposit nanoparticles on a surface. The plasmonic heat is generated when solar irradiates the coffee-ring. Because the coffee-ring diameter equals to the nanofluid droplet diameter, the coffee-ring diameter can be easily changed based on one's requirement. Moreover, the coffee-ring array can be created by evaporating multi-droplets, which are available by using a droplets jet generator. Second, the evaporation rate is only dependent on the coffee-ring parameters. One shall note that the coffee-ring particles generate heat, and the liquid is the heat receiver. The evaporation rate is insensitive to liquid film thickness and droplet contact angles. In order to verify the insensitive characteristic, a separate experiment was performed. It is found that the solar driven pure-water droplet evaporation on a prepared coffer-ring structure almost coincide with that of solar driven nanofluid droplet evaporation on a clean substrate, see Fig. S4 in Supplementary Information. This offers great convenience for solar energy applications.

5. Conclusions

When light irradiates nanofluid, nanoparticles will be re-assembled to affect the light absorption. Here, the solar-driven nanofluid droplet evaporation on a glass substrate is studied, which is different from that induced by substrate heating. We show that the droplet evaporation rates display a sharp increase regime and a constant regime. The two regimes are interfaced at a critical nanofluid concentration of ~10 ppm.

The solar driven nanofluid evaporation behaves distinct flow and temperature fields. A contact line region CLR and a bulk volume region BVR are identified. The radial flow from droplet center to contact line can be established by higher evaporation fluxes in CLR. The Marangoni flow is only limited in CLR, but cannot be well developed in BVR due to quasi-uniform temperatures over the whole droplet. The nanoparticles deposition forms the coffee-ring in CLR. CLR and BVR have different contributions to heat generations. Even though CLR only has 0.6–3.5% of the total droplet volume, it contributes more than 99% of the total electromagnetic energy absorption in visible region. Alternatively, BVR contributes almost all of the infrared energy absorption.

With increase of initial nanofluid concentrations, the droplet evaporation rates are raised due to more heat generation induced by enhanced nanoparticles deposition. The increased evaporation rates stop at a critical condition for sufficient nanoparticles deposition in CLR, corresponding to the critical concentration of ~10 ppm. Beyond the critical condition, extra nanoparticles are hidden beneath the effective nanoparticles layers, leading to a constant evaporation rate. In summary, we discover the critical concentration phenomenon and disclose the secret behind the phenomenon, which are of interest for both fundamental research and applications of solar energy utilization.

Conflict of interest

The authors declare no competing financial interest.

Acknowledgements

The authors acknowledge the support from the National Natural Science Foundation of China (51436004 and 51821004) and the Fundamental Research Funds for the Central Universities (2018ZD02 and 2018QN020).

Appendix A. Supporting information

Supplementary information associated with this article can be found in the online version at doi:10.1016/j.nanoen.2019.01.013.

References

[1] P.K. Jain, X. Huang, I.H. El-Sayed, M.A. El-Sayed, Noble metals on the nanoscale: optical and photothermal properties and some applications in imaging, sensing, biology, and medicine, Acc. Chem. Res. 41 (2008) 1578–1586.
[2] C. Zhang, M. Shao, F. Ning, S. Xu, Z. Li, M. Wei, D.G. Evans, X. Duan, Au nanoparticles sensitized ZnO nanorod@nanoplatelet core-shell arrays for enhanced photoelectrochemical water splitting, Nano Energy 12 (2015) 231–239.
[3] J.B. Lassiter, F. Mcguire, J.J. Mock, C. Ciracì, R.T. Hill, B.J. Wiley, A. Chilkoti, D.R. Smith, Plasmonic waveguide modes of film-coupled metallic nanocubes, Nano Lett. 13 (2013) 5866–5872.
[4] O. Nicoletti, F. De La Peña, R.K. Leary, D.J. Holland, C. Ducati, P.A. Midgley, Three-dimensional imaging of localized surface plasmon resonances of metal nanoparticles, Nature 502 (2013) 80.
[5] J.M. Bingham, J.N. Anker, L.E. Kreno, R.P. Van Duyne, Gas sensing with high-resolution localized surface plasmon resonance spectroscopy, J. Am. Chem. Soc. 132 (2010) 17358–17359.
[6] F. Le, D.W. Brandl, Y.A. Urzhumov, H. Wang, J. Kundu, N.J. Halas, J. Aizpurua, P. Nordlander, Metallic nanoparticle arrays: a common substrate for both surface-enhanced raman scattering and surface-enhanced infrared absorption, ACS Nano 2 (2008) 707–718.
[7] C. Ziming, W. Fuqiang, L. Huaxu, H. Shengpeng, L. Bo, T. Jianyu, L. Hongyang, Photon-absorption-based explanation of ultrasonic-assisted solar photochemical splitting of water to improve hydrogen production, Int. J. Hydrog. Energy 43 (2018) 14439–14450.
[8] R.K. Kannadorai, G.G.Y. Chiew, K.Q. Luo, Q. Liu, Dual functions of gold nanorods as photothermal agent and autofluorescence enhancer to track cell death during plasmonic photothermal therapy, Cancer Lett. 357 (2015) 152–159.
[9] H.M. Nguyễn, J. Lu, H. Goto, R. Maeda, Thermionic emission via a nanofluid for direct electrification from low-grade heat energy, Nano Energy 49 (2018) 172–178.
[10] G. Ni, N. Miljkovic, H. Ghasemi, X. Huang, S.V. Boriskina, C.-T. Lin, J. Wang, Y. Xu, M.M. Rahman, T. Zhang, G. Chen, Volumetric solar heating of nanofluids for direct vapor generation, Nano Energy 17 (2015) 290–301.
[11] Y. Wang, Q. Zhang, F. Huang, Z. Li, Y.-Z. Zheng, X. Tao, G. Cao, In situ assembly of well-defined Au nanoparticles in TiO_2 films for plasmon-enhanced quantum dot sensitized solar cells, Nano Energy 44 (2018) 135–143.
[12] S.A. Maier, Localized Surface Plasmons, in: S.A. Maier (Ed.), Plasmonics: Fundamentals and Applications, Springer, US, New York, NY, 2007, pp. 65–88.
[13] J.A. Scholl, A.L. Koh, J.A. Dionne, Quantum plasmon resonances of individual metallic nanoparticles, Nature 483 (2012) 421–427.
[14] Z. Wang, Z.M. Zhang, X. Quan, P. Cheng, A numerical study on effects of surrounding medium, material, and geometry of nanoparticles on solar absorption efficiencies, Int. J. Heat Mass Trans. 116 (2018) 825–832.
[15] H. Jin, G. Lin, L. Bai, A. Zeiny, D. Wen, Steam generation in a nanoparticle-based solar receiver, Nano Energy 28 (2016) 397–406.
[16] L. Zhou, Y. Tan, J. Wang, W. Xu, Y. Yuan, W. Cai, S. Zhu, J. Zhu, 3D self-assembly of aluminium nanoparticles for plasmon-enhanced solar desalination, Nat. Photonics 10 (2016).
[17] X. Wang, Y. He, X. Liu, L. Shi, J. Zhu, Investigation of photothermal heating enabled by plasmonic nanofluids for direct solar steam generation, Sol. Energy 157 (2017) 35–46.
[18] T. Yousefi, F. Veysi, E. Shojaeizadeh, S. Zinadini, An experimental investigation on the effect of Al2O3–H2O nanofluid on the efficiency of flat-plate solar collectors, Renew. Energy 39 (2012) 293–298.
[19] T. Yousefi, F. Veisy, E. Shojaeizadeh, S. Zinadini, An experimental investigation on the effect of MWCNT-H2O nanofluid on the efficiency of flat-plate solar collectors, Exp. Therm. Fluid Sci. 39 (2012) 207–212.
[20] R.A. Taylor, P.E. Phelan, T.P. Otanicar, A. Ronald, P. Ravi, Nanofluid optical property characterization: towards efficient direct absorption solar collectors, Nanoscale Res. Lett. 6 (2011) (225-225).
[21] E.P. Bandarra Filho, O.S.H. Mendoza, C.L.L. Beicker, A. Menezes, D. Wen, Experimental investigation of a silver nanoparticle-based direct absorption solar thermal system, Energy Convers. Manag. 84 (2014) 261–267.
[22] Q. He, S. Wang, S. Zeng, Z. Zheng, Experimental investigation on photothermal properties of nanofluids for direct absorption solar thermal energy systems, Energy Convers. Manag. 73 (2013) 150–157.
[23] A. De Risi, M. Milanese, D. Laforgia, Modelling and optimization of transparent parabolic trough collector based on gas-phase nanofluids, Renew. Energy 58 (2013) 134–139.
[24] H. Zhang, H.-J. Chen, X. Du, D. Wen, Photothermal conversion characteristics of gold nanoparticle dispersions, Sol. Energy 100 (2014) 141–147.
[25] M.T. Jamal-Abad, A. Zamzamian, E. Imani, M. Mansouri, Experimental study of the performance of a flat-plate collector using Cu–water nanofluid, J. Thermophys. Heat Transf. 27 (2013) 756–760.
[26] L. Kundan, P. Sharma, Performance evaluation of a nanofluid (CuO-H_2O) based low flux solar collector, Int. J. Eng. Res. 2 (2013) 108–112.
[27] M. Karami, M.A. Akhavan Bahabadi, S. Delfani, A. Ghozatloo, A new application of carbon nanotubes nanofluid as working fluid of low-temperature direct absorption solar collector, Sol. Energy Mater. Sol. Cells 121 (2014) 114–118.
[28] E.E. Michaelides, Transport properties of nanofluids. A critical review, J. Non-Equilib. Thermodyn. 38 (2013) 1–79.
[29] Y. Min, M. Akbulut, K. Kai, Y. Golan, J. Israelachvili, The role of interparticle and external forces in nanoparticle assembly, Nat. Mater. 7 (2008) 527–538.
[30] D. Jing, D. Song, Optical properties of nanofluids considering particle size distribution: experimental and theoretical investigations, Renew. Sust. Energy Rev. 78

(2017) 452–465.
[31] D. Song, M. Hatami, Y. Wang, D. Jing, Y. Yang, Prediction of hydrodynamic and optical properties of TiO_2 /water suspension considering particle size distribution, Int. J. Heat Mass Transf. 92 (2016) 864–876.
[32] M. Amani, P. Amani, A. Kasaeian, O. Mahian, W.-M. Yan, Two-phase mixture model for nanofluid turbulent flow and heat transfer: effect of heterogeneous distribution of nanoparticles, Chem. Eng. Sci. 167 (2017) 135–144.
[33] R.G. Larson, Transport and deposition patterns in drying sessile droplets, AICHE J. 60 (2014) 1538–1571.
[34] B. Sobac, D. Brutin, Thermal effects of the substrate on water droplet evaporation, Phys. Rev. E Stat. Nonlin. Soft Matter Phys. 86 (2012) 021602.
[35] H. Hua, R.G. Larson, Marangoni effect reverses coffee-ring depositions, J. Phys. Chem. B 110 (2006) 7090.
[36] R.G. Picknett, R. Bexon, The evaporation of sessile or pendant drops in still air, J. Colloid Interface Sci. 61 (1977) 336–350.
[37] R.D. Deegan, O. Bakajin, T.F. Dupont, G. Huber, S.R. Nagel, T.A. Witten, Capillary flow as the cause of ring stains from dried liquid drops, Nature 389 (1997) 827.
[38] J.Y. Kim, B.M. Weon, Evaporation of strong coffee drops, Appl. Phys. Lett. 113 (2018).
[39] L. Bansal, P. Seth, B. Murugappan, S. Basu, Suppression of coffee ring: (particle) size matters, Appl. Phys. Lett. 112 (2018).
[40] X. Zhong, A. Crivoi, F. Duan, Sessile nanofluid droplet drying, Adv. Colloid Interface Sci. 217 (2015) 13–30.
[41] D. Hanaor, M. Michelazzi, C. Leonelli, C.C. Sorrell, The effects of carboxylic acids on the aqueous dispersion and electrophoretic deposition of ZrO_2, J. Eur. Ceram. Soc. 32 (2012) 235–244.
[42] P.K. Jain, L. Kyeong Seok, I.H. El-Sayed, M.A. El-Sayed, Calculated absorption and scattering properties of gold nanoparticles of different size, shape, and composition: applications in biological imaging and biomedicine, J. Phys. Chem. B 110 (2006) 7238.
[43] M. Oksuz, H.Y. Erbil, Comments on the energy barrier calculations during “stick–slip” behavior of evaporating droplets containing nanoparticles, J. Phys. Chem. C 118 (2014) 9228–9238.
[44] Y. Fukatani, D. Orejon, Y. Kita, Y. Takata, J. Kim, K. Sefiane, Effect of ambient temperature and relative humidity on interfacial temperature during early stages of drop evaporation, Phys. Rev. E 93 (2016) 043103.
[45] A. Chandramohan, J.A. Weibel, S.V. Garimella, Spatiotemporal infrared measurement of interface temperatures during water droplet evaporation on a nonwetting substrate, Appl. Phys. Lett. 110 (2017) 041605.
[46] H. Masuda, S. Matsusaka, Powder Technology Handbook, Marcel Dekker, 2006.
[47] M.F. Modest, Chapter 10 - The Radiative Transfer Equation in Participating Media (RTE), in: M.F. Modest (Ed.), Radiative Heat Transfer, Third edition, Academic Press, Boston, 2013, pp. 279–302.
[48] B. Guillaume, Q. Romain, G.D.A.F. Javier, Nanoscale control of optical heating in complex plasmonic systems, ACS Nano 4 (2010) 709–716.

Dr. Jinliang Xu is the Dean of School of Mechanical and Power Engineering, North China Electric Power University, China. His research interest focuses on micro/nano heat transfer, micro energy system, and multiphase flow and heat transfer. He published more than 100 papers in recognized academic journals. He served as International conference chair or co-chair for several times in related area.

Xin Yan is a doctoral candidate in North China Electric Power University, China. His current research focuses on efficient solar energy utilization and nanoparticle plasmonic effect.

Dr. Guohua Liu received Ph.D. in Engineering of Thermophysics from Chinese Academy of Sciences in 2010. He obtained his 2nd Ph.D. in Micro and Nano Systems Technology at University of South-Eastern Norway (USN). Currently, he is a full professor at North China Electric Power University, China. His research interests center on development and assembly of nanostructured materials for energy applications.

Dr. Jian Xie is a post-doctor researcher from North China Electric Power University, China. His research interest focuses on micro/nano fluid and phase change heat transfer. He published more than 20 SCI papers and served as guest editor for some SCI journals. He was invited to give keynote pretentions for *International Conference on Nanomaterials & Nanotechnology* and *International Symposium of Fluids and Thermal Engineering*.